






REPORT

Filamin A mediates isotropic distribution of applied force across the actin network

Abhishek Kumar¹, Maria S. Shutova² , Keiichiro Tanaka¹ , Daniel V. Iwamoto³, David A. Calderwood^{3,4} , Tatyana M. Svitkina² , and Martin A. Schwartz^{1,4,5} 

Cell sensing of externally applied mechanical strain through integrin-mediated adhesions is critical in development and physiology of muscle, lung, tendon, and arteries, among others. We examined the effects of strain on force transmission through the essential cytoskeletal linker talin. Using a fluorescence-based talin tension sensor (TS), we found that uniaxial stretch of cells on elastic substrates increased tension on talin, which was unexpectedly independent of the orientation of the focal adhesions relative to the direction of strain. High-resolution electron microscopy of the actin cytoskeleton revealed that stress fibers (SFs) are integrated into an isotropic network of cortical actin filaments in which filamin A (FlnA) localizes preferentially to points of intersection between SFs and cortical actin. Knockdown (KD) of FlnA resulted in more isolated, less integrated SFs. After FlnA KD, tension on talin was polarized in the direction of stretch, while FlnA reexpression restored tensional symmetry. These data demonstrate that a FlnA-dependent cortical actin network distributes applied forces over the entire cytoskeleton–matrix interface.

Introduction

Live cells sense and respond to externally generated stretch, shear, and compression, and internal changes in actomyosin contractility (Geiger et al., 2009). Applied forces can vary by several orders of magnitude and on temporal scales from sub-seconds to days. Immediate responses are thought to mainly involve protein conformational changes that lead to changes in binding affinities or enzymatic activity (Vogel and Sheetz, 2006; Hsu et al., 2010; Humphrey et al., 2014; Goult et al., 2018). Ultimately, these events regulate signaling pathways, gene expression, and changes in cell and tissue phenotype. Over the past decade, our molecular understanding of mechanotransduction has rapidly expanded. However, major questions remain about how applied forces are distributed and act upon force-sensitive molecules.

The cell–ECM interface is a critical location for mechanical regulation. The focal adhesion (FA) protein talin is a key component of this linkage and a key player in mechanotransduction. Talin contains an N-terminal FERM domain that binds to integrin β subunit cytoplasmic tails. Talin's C-terminus is comprised of a rod domain consisting of 13 helix bundles with two binding sites for F-actin: ABS2 (actin binding site 2) between residues 951 and 1327 and ABS3 near C-terminal between

residues 2300 and 2541 (Himmel et al., 2009; Atherton et al., 2015; Klapholz and Brown, 2017). These helix bundles were found to open under force, exposing cryptic vinculin-binding sites, such that tension induces vinculin recruitment and reinforcement of the link to actin (Patel et al., 2006; del Rio et al., 2009; Hirata et al., 2014). Previous studies measuring force across talin showed that talin tension requires actomyosin contractility and is modulated by ECM stiffness (Austen et al., 2015; Kumar et al., 2016, 2018).

In vivo, most, if not all, cells respond to mechanical stretch. These effects are most prominent in cardiac cardiomyocytes and fibroblasts, vascular endothelial and smooth muscle cells, intestinal smooth muscle, and multiple cell types in the lung, where mechanical stretch plays major roles in development and physiology. In vitro, cyclic uniaxial mechanical stretching of nonmuscle cell types induces orientation perpendicular to the direction of stretch, with similar orientation of FAs and the actin cytoskeleton (Wang et al., 2004; Kaneko et al., 2009; Hsu et al., 2010; Nagayama et al., 2012). Presumably, these events are a consequence of forces transmitted through the integrin–talin–actin linkage, but our understanding of how these forces are transmitted is limited. The goal of this study was to investigate

¹Yale Cardiovascular Research Center, Yale University School of Medicine, New Haven, CT; ²Department of Biology, University of Pennsylvania, Philadelphia, PA; ³Department of Pharmacology, Yale University, New Haven, CT; ⁴Department of Cell Biology, Yale University, New Haven, CT; ⁵Department of Biomedical Engineering, Yale University, New Haven, CT.

Correspondence to Martin A. Schwartz: martin.schwartz@yale.edu; Abhishek Kumar: a.kumar@yale.edu.

© 2019 Kumar et al. This article is distributed under the terms of an Attribution–Noncommercial–Share Alike–No Mirror Sites license for the first six months after the publication date (see <http://www.rupress.org/terms/>). After six months it is available under a Creative Commons License (Attribution–Noncommercial–Share Alike 4.0 International license, as described at <https://creativecommons.org/licenses/by-nc-sa/4.0/>).

the role of talin in cell responses to strain using our previously described talin tension sensor (TS). Our results unexpectedly showed that polarized forces from uniaxial stretch are transmitted to talin in a depolarized way. Further analysis showed that an actin cytoskeletal network that requires filamin A (FlnA) redistributes the applied force.

Results and discussion

Talin tension within FAs increases after uniaxial sustained stretch

To apply uniaxial stretch to live cells, we built custom uniaxial stretchers by 3D printing (Fig. 1, A and B). The magnitude of stretch was precisely controlled using break pins located on the base of stretcher. Strain profiles with polydimethylsiloxane (PDMS) membranes were determined by imaging fluorescent beads before and after stretch in the central region of the stretcher that was used for cell imaging (Fig. S1 A). Bead tracks, obtained using particle imaging velocimetry (PIV; Fig. S1 B), showed that displacements parallel and perpendicular to the direction of stretch were uniform in these regions (Fig. S1, C and D) as shown previously (Shao et al., 2013). For 10% stretch along the x axis, there was compression of $3.3 \pm 0.2\%$ along the y axis, consistent with previous results (Shao et al., 2013). The force on talin was measured using the previously characterized fluorescence resonance energy transfer (FRET)-based TS in which the donor fluorophore, EGFP, is linked to an acceptor fluorophore, tagRFP through a 40-amino acid spring-like peptide (Kumar et al., 2016, 2018). Tension extends the spring and decreases FRET efficiency in a well-defined way (Grashoff et al., 2010). In Talin-TS, this module is inserted into the flexible linker between talin's head and rod regions, where it registers force between the integrin binding site in the N-terminus and F-actin- and vinculin-binding sites in the C-terminus (Fig. S1 E). The control sensor, talin-CS, with the module affixed to the C-terminus, localizes similarly but does not register tension (Fig. S1 E).

Talin1^{-/-} mouse embryonic fibroblasts transfected with talin-TS were plated on fibronectin-coated ~400- μ m-thick PDMS membranes assembled into the stretch device. Well-spread cells 6 h after plating were left untreated or uniaxially stretched by 10% and then immediately fixed in the same state with 4% paraformaldehyde. The total time taken to manually turn the screw and add fixative is ~10 s. PDMS membranes were mounted in their stretched or unstretched state on a glass slide and imaged, and the FRET index within FA calculated. Fig. 1 C shows a pseudo-colored FRET index map of talin tension within FA in unstretched and stretched cells with corresponding color bar (high FRET index value indicates low tension, and low FRET index value indicates high tension). Immediately after 10% stretch, FRET index within FA reproducibly decreased, indicating higher tension on talin (quantified in Fig. 1 D). As expected, FRET index for the talin-CS control did not change after 10% stretch (Fig. S1, F and G).

We next examined the stretch response as a function of FA orientation relative to the direction of stretch. Mean FRET index per FA in peripheral FAs was plotted against absolute FA angle, with 0° being the direction of stretch. When FAs oriented at

angles within $\pm 30^\circ$ of 0 or 90° were binned and classified as parallel or perpendicular, respectively, there was no significant difference in FRET index after stretch (Fig. 1, E and F). This result was surprising given that FAs are connected to actomyosin stress fibers (SFs) that are the main source of tension on talin (Kumar et al., 2016). Actin bundles in the direction of stretch will increase in length, whereas those parallel will not. This finding prompted us to consider whether there are additional cytoskeletal networks that contribute to force transmission.

A FlnA-dependent network spatially integrates actin SF bundles

Ultrastructural analysis of the actin cytoskeleton in cultured cells revealed an isotropic network of cortical filaments beneath the plasma membrane into which SF bundles are integrated (Svitkina, 2007, 2018; Eghiaian et al., 2015). This network is therefore positioned to mediate the redistribution of forces observed above. FlnA is a major actin cross-linker in a majority of cell types including fibroblasts and, because of its length and flexibility, is a likely candidate for connecting SFs into the isotropic actin network (Zhou et al., 2010; Razinia et al., 2012). Indeed, platinum replica immuno-EM (PREM) in combination with 18-nm immunogold staining of FlnA revealed FlnA on the actin cytoskeleton throughout the cell but with higher frequency at points of intersection between SF bundles and the isotropic network (Fig. 2, A–D). Quantitative analysis of the gold particle localization within SFs revealed that $62.9 \pm 8.0\%$ of the particles were localized within immediate proximity of sites where isotropic actin filaments intersected the SF at high ($>30^\circ$) angles, whereas $37.1 \pm 8.0\%$ were found on the parallel actin filament bundles >18 nm from an intersection (Fig. 2 E). To test whether this preferential localization of FlnA at the sites of intersection was specific, we repeated the quantification after rotating the PREM images by 180° but keeping the gold particle positions fixed. Particle counts at sites of intersection versus along SFs were $46.6 \pm 8.8\%$ and $53.4 \pm 8.8\%$, respectively, which was significantly different from the unrotated images (P value = 0.0007; Fig. 2 E). In some cases, the same actin filament was visualized as a component of a SF but then diverged or frayed to join the meshwork of loose actin filaments (Fig. 2 C, inset).

SFs become less interconnected after FlnA knockdown (KD)

We next tested the effect of FlnA KD on cell and FA morphology and actin organization using lentiviral infection of shRNA in NIH3T3 fibroblasts, followed by selection in puromycin. Immunofluorescence (IF) imaging (Fig. 3 A) and immunoblotting (Fig. 3 B) using FlnA antibody showed that FlnA was reduced by $>97\%$ (Fig. S1 J). Confocal imaging of phalloidin-labeled F-actin showed no obvious changes in actin organization between scrambled (scr) and FlnA shRNA cells (Fig. 3 A; Feng et al., 2006). We further labeled FAs by transfecting cells transiently with talin-TS (Fig. 3 C) to assess changes in adhesion morphology. Cell area (Fig. S1 K), FA area (Fig. S1 L), and FA aspect ratio (Fig. S1 M) were not significantly different after FlnA KD. Further, the FA orientation with respect to cell orientation was no different after FlnA KD (Fig. S1 N). Photobleaching small regions

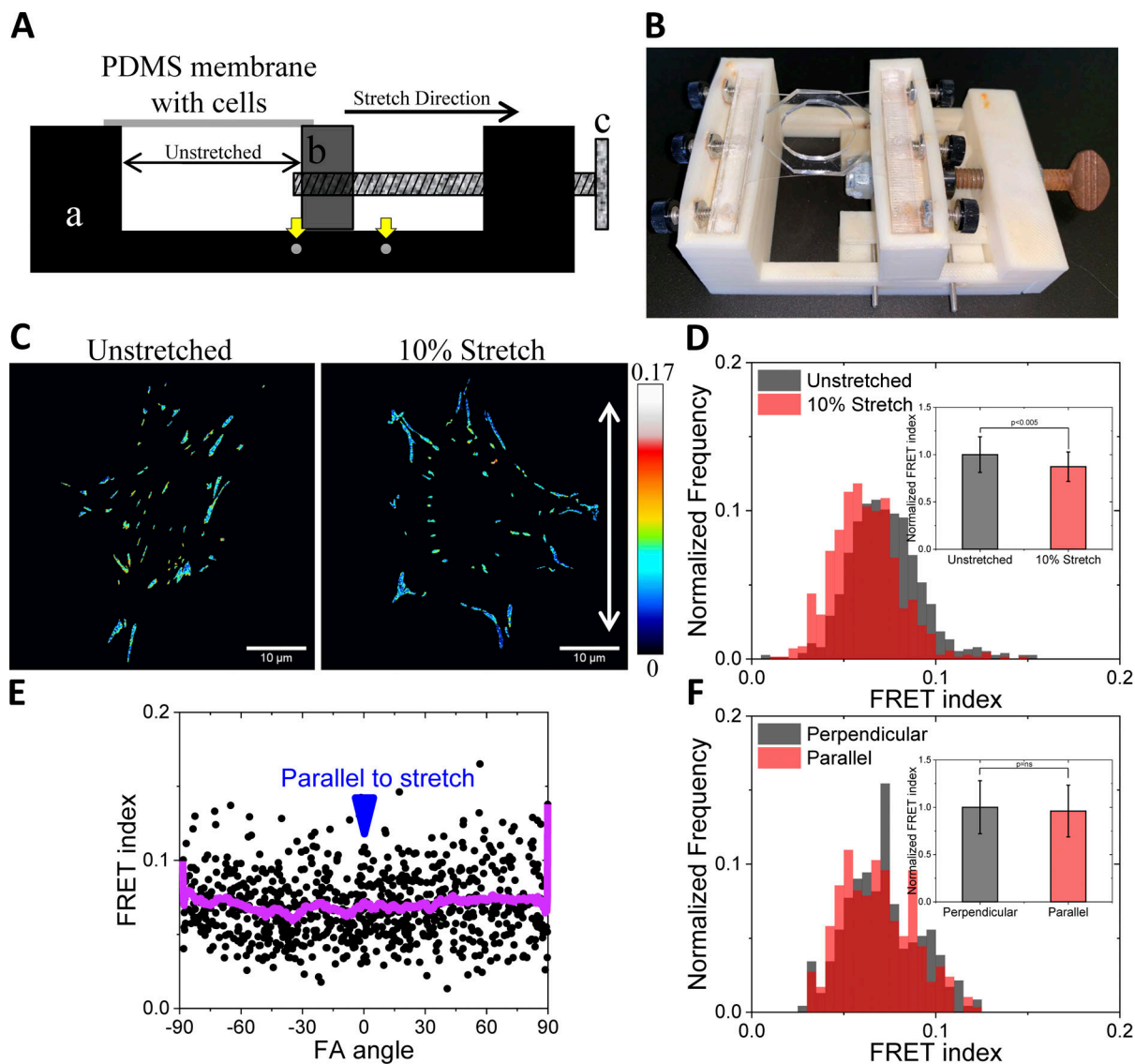


Figure 1. Isotropic increase in talin tension after uniaxial sustained stretch. (A) Schematic of uniaxial stretch device. Thick black arrow shows the direction of stretch. Black denotes the fixed part while the movable part is in gray. Yellow arrows indicate break pins for 10% stretch. (B) Photograph of stretcher with thin PDMS membrane and thick ring attached to create the well. (C) Representative FRET index map of talin-TS in FA in unstretched (left) and 10% stretched (right) membranes. The color bar represents the FRET index values where high FRET (red/white) indicates low tension while low FRET (blue) indicates high tension. White arrow shows the direction of stretch. Scale bars, $10 \mu\text{m}$. (D) Histogram of mean FRET index per FA in unstretched and 10% stretched cells. Inset: Average FRET index normalized to the unstretched values for each experiment ($n = 756$ and 701 FAs from 48 and 36 cells in unstretched and 10% stretched state, respectively). (E) Plot of FRET index versus FA angle relative to direction of stretch for peripheral adhesions. Blue arrowhead indicates the direction of stretch ($n = 830$ peripheral FAs from 36 cells stretched by 10%). The purple line shows the smoothed plot obtained by 50-point adjacent averaging. FAs were categorized as parallel ($0^\circ \pm 30^\circ$) or perpendicular (60° to 90° and -90° to -60°). (F) Histogram of mean FRET index per FA for perpendicular and parallel FAs in 10% stretched cells. Inset: Average FRET index normalized to perpendicular FAs within each experiment ($n = 233$ and 292 FAs for perpendicular and parallel FAs, respectively, from 36 cells). Four independent experiments gave similar results. Error bars represent SD.

within FAs showed no detectable effect of FlnA KD on exchange dynamics and mobile fractions for talin (Fig. S1 O) and vinculin (Fig. S1 P). Western blotting of whole cell lysate for integrin $\beta 1$, talin, vinculin, paxillin, phosphorylated paxillin (Y31), phosphorylated FAK (Y397), tensin1, and actin along with tubulin and GAPDH as loading controls showed no change after FlnA KD (Fig. S1, Q–T). However, IF imaging of the same FA proteins within individual FA sites revealed some effects (Fig. S2). Integrin $\beta 1$ (Fig. S2 A, i and ii) was higher within FAs after FlnA KD, and there were modest increases in FA localization of talin (Fig. S2 B,

i and ii), tensin1 (Fig. S2 G, i and ii), and phosphorylated FAK (Fig. S2 F, i and ii). FA localization of vinculin (Fig. S2 C, i and ii), phosphorylated paxillin (Fig. S2 E, i and ii), and actin (Fig. S2 H) was slightly decreased after FlnA KD, with total paxillin (Fig. S2 D, i and ii) showing no change. These changes are consistent with and likely due to the previously observed impaired mobility upon FlnA KD (Baldassarre et al., 2009).

Actin organization was then examined at high resolution by PREM. In control NIH3T3 cells, actin SFs are comprised of thinner interconnected actin sub-bundles that diverge and fuse

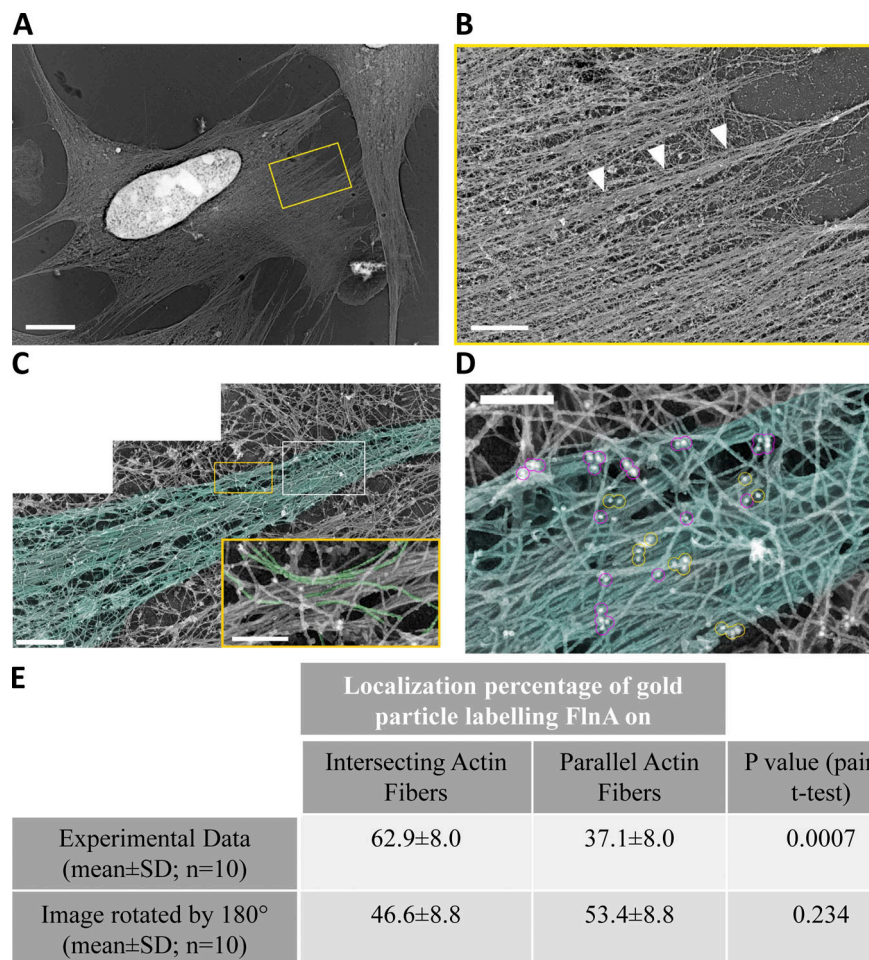


Figure 2. A FlnA-dependent network spatially integrates actin SFs. (A–D) Immunogold PREM at increasing magnifications of control scr shRNA NIH3T3 cells. **(A)** Whole-cell image. Scale bar, 10 μ m. **(B)** Zoomed-in image of boxed region in A. Scale bar, 2 μ m. Arrowheads point to a putative FA region with bundled actin. **(C)** Zoomed-in view of SF region shown in B. Scale bar, 0.5 μ m. Inset: Zoomed-in image of yellow boxed region showing the trace of actin filaments visualized as a component of a SF which diverged to join the meshwork of loose actin filaments. **(D)** Zoomed-in image of white boxed region marked in C showing FlnA immunogold particles on intersecting actin filaments (purple circles) or parallel actin filaments (yellow circles). Scale bar, 200 nm. **(E)** Quantification of the percentage of gold particle labeling FlnA localized on intersecting and parallel actin filaments within the region of a SF ($n = 4,234$ gold particles from 10 cells).

throughout the length of the SF (Fig. 3, D and E; and Fig. S3 A, i and ii). Importantly, SFs with different orientations, for example, coming from two neighboring protrusions, typically merged to form arc-like structures (Fig. 3, D and E; and Fig. S3 A, i and ii). These SFs thus appeared mechanically connected via the integrating isotropic network. However, upon FlnA depletion, SF interconnectivity decreased. The SFs appeared more discrete (Fig. 3, F and G; and Fig. S3 B, i and ii) with the individual actin bundles less “fluffy” and more easily traced for long distances (Fig. 3, F and G; and Fig. S3 B, i and ii). SFs coming from different directions more often overlapped without the interconnecting network (quantified in Fig. 3 H). SFs were also more compact, as quantified by counting the number of individual actin bundles intersected by a line scan drawn perpendicular to the direction of SFs (Fig. S3 A, ii and iii; and Fig. S3 B, ii and iii). In line scans, actin bundles correspond to high-intensity peaks with values above the mean intensity level of the image. Although intensity fluctuations also occur within the bundle, they remain above the mean. These high-intensity peaks alternated with low-intensity regions with values below the image mean intensity due to gaps between the bundles. In control cells, a large number of actin bundles alternating with small gaps was observed per line scan length, as compared with discrete and less numerous bundles with larger but fewer gaps in FlnA KD cells (Fig. 3 I;

and Fig. S3 A, iii, control cell; and Fig. S3 B, iii, FlnA KD cell; see Materials and methods section for more details).

Talin tension after FlnA KD

Talin-TS was then expressed in control and FlnA KD cells, and FRET measured as above. Pseudo-colored FRET index map of talin-TS (Fig. 3 J and quantification in Fig. 3 K) showed that tension on talin is on average slightly higher after FlnA KD but that the pixelwise FRET index distributions substantially overlapped (Fig. 3 L). We next examined cell responses to uniaxial stretch. The scr control and FlnA shRNA cells were plated on elastic substrates and subjected to uniaxial stretch as before. Similar to untransfected cells (Fig. 1), scr shRNA cells showed an increase in talin tension after stretch (Fig. S3 C) that was independent of orientation relative to the direction of strain (Fig. 4 A, i–iii). By contrast, in FlnA KD cells, talin in FAs oriented parallel to the strain showed a larger decrease in FRET index (increase in tension) compared with perpendicular FAs (Fig. 4 B, i–iii). Mean FRET index per FA versus FA orientation angle is shown in Fig. 4, A and B, ii, for scr and FlnA KD cells, respectively. Thus, FlnA is required for the depolarization of tension on talin. Cell orientation in scr and FlnA KD cells when unstretched, immediately and 5 min after 10% stretch, was random under all of these conditions (Fig. S3 D). Rescue by reexpression of SNAP-tagged WT full-length human FlnA in KD

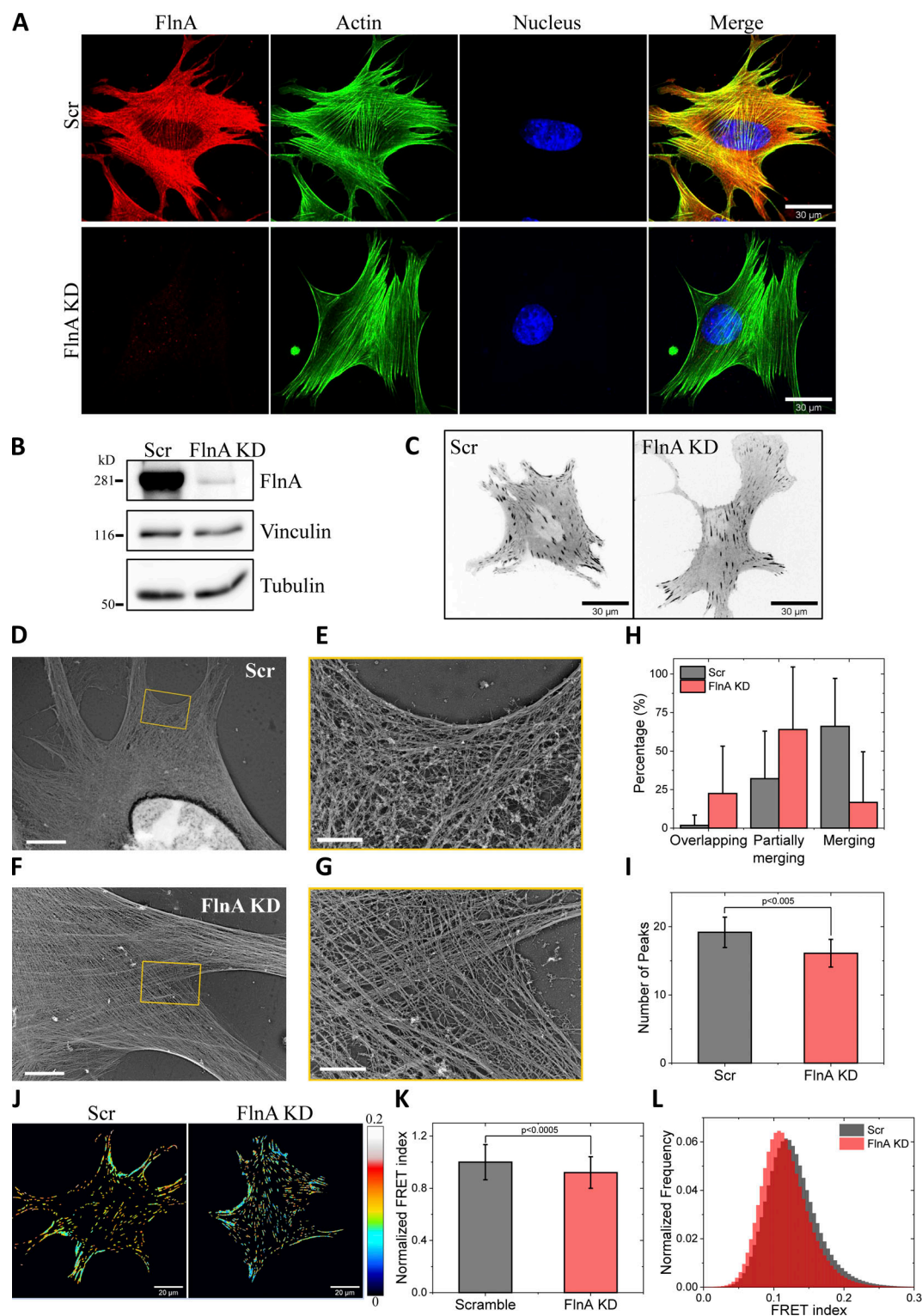


Figure 3. SFs become less interconnected after FlnA KD. (A) Representative fluorescence images of scr and FlnA shRNA NIH3T3 cells showing FlnA staining (red), actin (green), nuclei (blue), and merged images. Scale bars, 30 μ m. (B) Representative WB for FlnA, vinculin, and tubulin in scr and FlnA shRNA cells. (C) Representative inverted tagRFP intensity images of talin-TS-transfected scr and FlnA KD cells. Scale bars, 30 μ m. (D–G) Representative PREM images of scr (D and E) and FlnA KD (F and G) cells. Respective zoomed-in images (E and G) of the boxed regions in D and F. Scale bars, 5 μ m in D and F; and 1 μ m in E and G. (H) Quantification of overlapping, partially merging and merging actin fibers in scr (gray) and FlnA KD (light red) cells. $n = 14$ and 20 for scr and FlnA KD cells, respectively. $P < 0.05$, obtained from Student's t test. (I) Number of peaks (SFs count) per micron line scan length in scr and FlnA KD cells. $n = 14$ cells each. Error bars represent SD. (J) Representative FRET index maps of talin-TS-transfected NIH3T3 fibroblasts in scr (left) and FlnA KD (right) cells. Pseudocolor scale indicates FRET index values. Scale bars, 30 μ m. (K) Average FRET index normalized to scr in each experiment. Error bars represent SD. $n = 86$ and 78 cells for scr and FlnA cells, respectively. (L) Histogram of pixelwise FRET index for the same data.

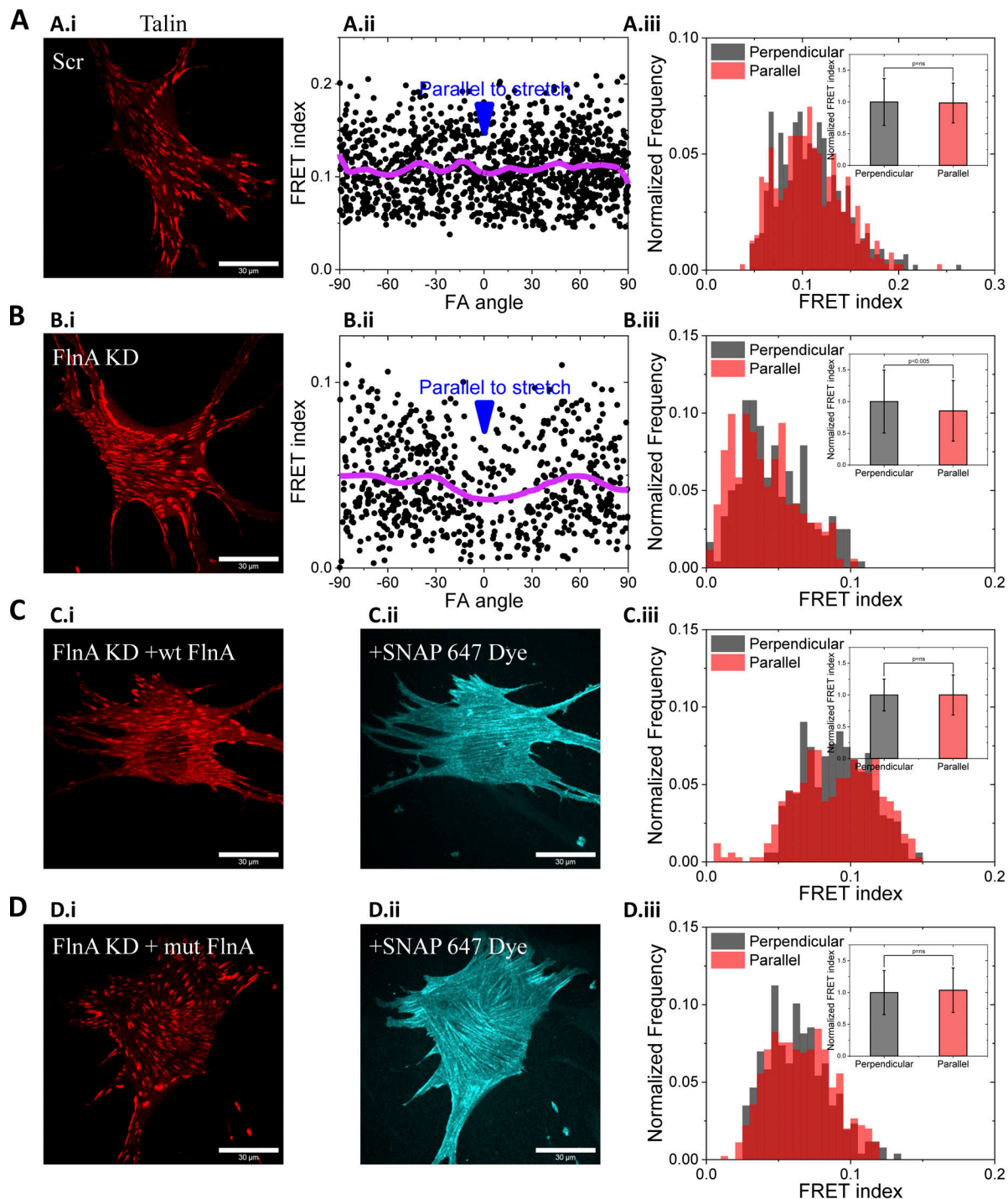


Figure 4. Effect of FlnA KD on tension polarity. (A–D, i) Representative images of talin-TS (tagRFP) images. (A and B, ii) Mean FRET index versus FA angle/orientation for peripheral adhesions in stretched scr (A, ii) and FlnA KD (B, ii) cells. Blue arrowhead indicates the direction of stretch with respect to image axis ($n = 1,273$ and 695 peripheral FAs for A, ii; and B, ii, respectively). Purple line is smoothed plot obtained by 50-point adjacent averaging. (C–D, ii) Alexa Fluor 647–conjugated SNAP dye to label SNAP-tagged WT FlnA (C, ii) or integrin binding–deficient FlnA (D, ii). (A–D, iii) Histogram of average FRET index per FA for perpendicular and parallel FAs in 10% stretched condition. Inset to A–D, iii: Mean FRET index normalized to the perpendicular FAs within each cell. (A–D) Cells with scr (A), FlnA KD (B), and FlnA KD rescued with either WT full-length human FlnA (C) or integrin binding–deficient (I2092C/I2283C) FlnA (D). $n = 441$ and 398 , 240 and 171 , 524 and 335 , and 258 and 450 perpendicular and parallel FAs for A, iii; B, iii; C, iii; and D, iii, respectively. Error bars represent SD.

cells restored the depolarization (Fig. 4 C, i–iii; FlnA labeled with SNAP-tagged Alexa Fluor 647 dye in Fig. 4 C, ii; and Fig. 4 D, ii). FlnA also binds to integrin β cytoplasmic domains, potentially providing another link to F-actin (Kiema et al.,

2006). To test whether this interaction contributes to depolarization of force, we rescued FlnA KD cells with SNAP-tagged I2092C/I2283C FlnA, which is deficient in integrin binding (Kiema et al., 2006). This mutant was equally effective at

restoring the polarized response in talin tension upon uniaxial stretch (Fig. 4 D, i–iii).

These studies yielded the unexpected result that an anisotropic stretch led to an isotropic increase in tension on talin across the whole cell. This depolarized response required the actin cross-linker FlnA but did not require FlnA binding to integrins. These results fit well with ultrastructural visualization of a cortical actin network that connects and integrates SFs with different orientations/directions (Svitkina, 2007, 2018). Here, we find that FlnA localizes preferentially to sites where the mesh-like isotropic actin cytoskeleton links to actin SF bundles and that FlnA depletion disrupts connectivity between SFs from different directions without significant changes in cell spread area or FA area and aspect ratio (Fig. 3; Baldassarre et al., 2009). Results from a conformation-sensitive FlnA biosensor suggested that FlnA in cells is under tension (Nakamura et al., 2014). We speculate that when cells are stretched, tension increases in both the actin SFs and the isotropic cortical actin network according to their viscoelasticity. As an essential load-bearing element between these networks, FlnA would thus play a major role in transferring tension between them to redistribute and equalize forces on FAs.

These results may be relevant to the ability of FlnA to promote cell survival under mechanical load (Pinto et al., 2014). Cyclic strain increases expression of FlnA, which promotes rigidity and mechanical stability of the cortical actin cytoskeleton (D'Addario et al., 2001; Zhou et al., 2010; Razinia et al., 2012). Force application was found to rapidly decrease plasma membrane potential, which, in FlnA-deficient cells, contributed to irreversible cell depolarization and cell death (Kainulainen et al., 2002). The ability of FlnA to redistribute applied forces is likely to contribute to its function in promoting cell survival under strain.

While tension on talin may be independent of strain direction, the subsequent evolution of the cytoskeleton need not be. During sustained uniaxial stretch, there is an orientation-independent rapid induction of FA growth/reinforcement that is followed by orientation-dependent slow FA disassembly, an important step for enforcing alignment of cells perpendicular to the direction of stretch (Faust et al., 2011; Chen et al., 2013). FAs grow along actin SFs that serve as scaffolds for recruitment of FA components, a role that is distinct from SF contractility (Choi et al., 2008). Thus, our findings do not conflict with results that parallel and perpendicular FAs remodel differently in response to uniaxial stretch (Chen et al., 2013) and align perpendicular to the direction of cyclic uniaxial stretch (De et al., 2007; Faust et al., 2011). Indeed, detailed imaging suggested that remodeling begins with differential responses of the SFs rather than the FAs (Lee et al., 2010), while SFs show remodeling events in response to stretch at regions far from FAs (Smith et al., 2010). Thus, despite the lack of polarity at the level of talin tension, the orientation of SFs may therefore confer polarized cell responses to applied forces.

In summary, these results reveal a key role for FlnA in integrating FAs and SFs with the isotropic cortical actin network to mediate rapid distribution of forces and thereby modulate cell

responses. Further understanding of this “asymmetry breaking” process and its implications for cell mechanics and signaling will be important for understanding both physiological and pathological responses to force, and diseases such as aneurysm and developmental disorders related to filamin mutations (Zhou et al., 2010; Razinia et al., 2012).

Materials and methods

Cell culture and plasmid transfection

Talin1^{-/-} cells (Priddle et al., 1998) were cultured in DMEM/F12 (Gibco) with 10% FBS (Gibco), penicillin-streptomycin (Gibco), β-mercaptoethanol (5 μl in 500 ml; Sigma-Aldrich), and sodium bicarbonate (8 ml of 7.5% [weight by volume] in 500 ml media; Sigma-Aldrich). NIH3T3 (ATCC) fibroblasts were cultured in DMEM (Gibco) with 10% FBS (Sigma-Aldrich) and penicillin-streptomycin (Gibco). Talin-TS was as described (Kumar et al., 2016). SNAP-tagged WT and integrin binding-deficient mutant FlnA constructs were derived from corresponding plasmids WT (pcDNA3-FlnA-GFP) and FlnA with mutations I2092C/I2283C (Kiema et al., 2006; Lad et al., 2007) by replacing EGFP with the sequence encoding SNAP. All plasmids were constructed using PCR-based oligonucleotide synthesis and Gibson cloning and were confirmed by DNA sequencing. Talin1^{-/-} mouse embryonic fibroblast and NIH3T3 cells were transfected with Talin-TS and/or SNAP-tagged FlnA vectors using Jetprime reagent (Polyplus) and Lipofectamine 2000 (Invitrogen), respectively, according to the manufacturers' protocol.

Antibody and dye labeling

The following primary antibodies were diluted in TBS with 0.1% Tween 20 (Sigma-Aldrich) and used overnight at 4°C: rabbit polyclonal anti-human FlnA antibody, which cross-reacts with mouse FlnA (1:1,000 for Western blot [WB] and 1:200 for IF; Kiema et al., 2006; Heuzé et al., 2008; Iwamoto et al., 2018); mouse vinculin (1:2,000 for WB and 1:1,000 for IF; clone hVIN-1; V9131; Sigma-Aldrich), mouse tubulin (1:2,000 for WB; clone DM1a; T9026; Sigma-Aldrich), mouse talin (1:2,000 for WB and 1:500 for IF; clone 8d4; T3287; Sigma-Aldrich), integrin β1 (1:200 for WB; Chan and Hemler, 1993), Alexa Fluor 647-conjugated Armenian hamster integrin β1 (1:1,000 for IF; clone HMβ1-1; #102214; Biolegend); rabbit paxillin (1:2,000 for WB and 1:500 for IF; ab32084; Abcam); rabbit phosphorylated Y31 paxillin (1:500 for WB and 1:400 for IF; 44-720G; Invitrogen); rabbit tensin1 (1:2,000 for WB and 1:500 for IF; SAB4200283; Sigma-Aldrich); rabbit phosphorylated Y397 FAK (1:2,000 for WB and 1:500 for IF; #3283; Cell Signaling Technology); goat anti-actin (1:2,000 for WB; C-11; sc-1615; Santa Cruz Biotechnology); and rabbit GAPDH (1:2,500 for WB; #2118; Cell Signaling Technology). Actin was labeled using Alexa Fluor 647-conjugated phalloidin (1:200 in PBS; Molecular Probes). Nuclei were labeled using Hoechst 33342 (1:1,000 in PBS; Molecular Probes). SNAP-tagged filamin was labeled using Alexa Fluor 647-conjugated cell-permeable SNAP dye (1:200 in cell culture media; New England Biolabs).

FlnA KD

FlnA was depleted using lentivirus targeting mouse shRNA (sequence 5'-CTAGAAGCTCCCATGGCAATG-3') in pLKO.1 vector. For lentivirus production, HEK 293Tx cells (ATCC) were plated overnight at 70% confluency in 10-cm dishes and transfected with either scr or FlnA shRNA plus equal amounts of the two third-generation packaging plasmids (Addgene) using Lipofectamine 2000 (Invitrogen) according to the manufacturer's protocol. Transfection media were replaced after 6 h with standard culture media. Lentivirus particle-rich media were collected after 48 h and centrifuged at 300 *g* at 4°C for 15 min. For infection, this supernatant plus 4 µg/ml polybrene was added to NIH3T3 cells plated overnight at 70% confluency. 1 d later, infection media were replaced with fresh growth medium. After 2 d, cells were replated, and the next day, 6 µg/ml puromycin was added. Cells were used after 5 d of selection, which was sufficient to kill control, uninfected cells.

Stretching cells

The uniaxial stretcher was fabricated by 3D printing (Yale Center for Engineering Innovation and Design, New Haven, CT) as shown in Fig. 1, A and B. Membranes were made from PDMS Sylgard 184 (Dow Corning) by thoroughly mixing the base and curing agent in a 10:1 ratio. Thin (~400 µm) membranes used ~7.5 g in a 15-cm Petri plate; thick rings for creating wells used ~45 g in a 10-cm Petri plate. PDMS was polymerized at 80°C for 3 h for curing. Membranes (29 mm × 44 mm) were cut and attached to the stretcher. Thick PDMS rings with inner diameters of 19 mm was kept on the membranes to create wells to hold the cells and culture medium. The devices were UV sterilized for 20 min in a tissue culture hood and then coated with 10 µg/ml fibronectin. Cells were plated on the membrane at low density for 6 h before stretching. The thick PDMS ring was removed, stretch was applied, and cells were immediately fixed using 4% paraformaldehyde in PBS. Cells were washed four or five times with PBS. The PDMS membranes (in their stretched or unstretched state) were glued to a plastic slide, which was then glued to a glass slide for stability. Cells were mounted using Prolong Gold mounting medium, and the PDMS membranes were cut from the stretcher and imaged within 2–3 d.

Calibration of uniaxial stretcher device

To calibrate the strain profile of the uniaxial stretcher, 2-µm yellow-green fluorosphere carboxylate fluorescent beads (Invitrogen) were adhered to the PDMS membrane assembled in the device as follows: the PDMS was silanized by adding 300 µl of (3-aminopropyl) triethoxysilane (Sigma-Aldrich) at room temperature for 15 min. Bead solution was prepared by mixing 5 ml borate buffer (0.76 g sodium tetraborate decahydrate and 1 g boric acid [Sigma-Aldrich] in 200 ml water, stirred at 70°C until clear, pH adjusted to 7.4 by adding more boric acid and stirring), 50 µl N-(3-dimethylaminopropyl)-N'-ethylcarbodiimide hydrochloride (EDC; Sigma-Aldrich) solution (5 mg EDC in 500 µl water), and 2 µl of stock bead suspension. 1 ml freshly prepared bead solution was placed on the freshly silanized membrane and incubated for 2 h at room temperature. The membranes were thoroughly washed with water, and

the density of the beads was checked under a fluorescence microscope.

For characterization, the device was kept upside down on the microscope slide holder, and four different regions of interests (1,785 µm × 1,785 µm), each within the central region of the well on the membrane, were imaged using 4× objective (0.2 NA; Plan Apo Nikon) before and after 10% stretch. Paired bead images were aligned using Template Matching plugin in ImageJ (National Institutes of Health) by choosing a 250 pixel × 250 pixel region in the center of image. Averaged relative beads displacement vector was determined using PIV using the Iterative PIV (cross-correlation) plugin in ImageJ. Three-pass PIV analysis was performed using 256 × 256, 128 × 128, and 64 × 64 pixel interrogation window size. Post-PIV processing was performed using the normalized median test, and invalid vectors were replaced by median vectors. PDMS has a Poisson's ratio of ~0.5, which means that to conserve the volume of the total material under a given stretch, there will be compression close to 50%. However, the profile of stretch and compression depends on the aspect ratio of the membrane used and the boundary conditions. As shown earlier (Shao et al., 2013), the central region has a uniform strain profile that is also found our custom-built uniaxial stretcher. For 10% stretch along the x axis, there is compression of $3.3 \pm 0.2\%$ along the y axis. Both stretch and compression strain profiles are uniform in the areas of the PDMS used for plating cells and imaging before/after stretch.

FA threshold and error in angle estimation

FA segmentation was performed as described before (Kumar et al., 2016, 2018). Images were individually checked manually after segmentation. To estimate the error in angle calculation, four different thresholding conditions were applied to FAs within the same cell, and the mask from each condition was used to get the angle of the ellipse that best fits the mask using ImageJ. Fig. S1 H shows inverted intensity image of FAs from a cell along with four different threshold masks (Fig. S1 I, upper panel) in decreasing order of lower-intensity cut-off and corresponding ellipse (Fig. S1 I, lower panel) that best fits these FA masks. The angle of the FA was estimated from the major axis of these ellipse. The average SD in angle measurement was determined to be $1.2 \pm 0.7^\circ$ from *n* = 10 FAs. FAs oriented at angles within $\pm 30^\circ$ of 90° and 0° were segregated into perpendicular and parallel; thus, angle estimation and FA classification are very robust without any overlap between the two categories.

Imaging and analysis

FRAP experiments were performed on a microscope (Eclipse Ti; Nikon) equipped with a spinning disk confocal imaging system (Ultraview Vox; PerkinElmer) and an electron-multiplying charged-coupled device camera (C9100-50; Hamamatsu Photonics), using a 100×, 1.4 NA oil objective. Cells were maintained at 37°C with humidity and CO₂ control. Images were acquired using Velocity 6.6.1 software. Three prebleach images at 2-s intervals and then a laser pulse at 100% power of the 488-nm line were used to bleach a circular region of 1 µm diameter. Time-lapse images were then acquired every 5 s for 2.5 min. Images were corrected for photobleaching during image

acquisition, and normalized FRAP curves were plotted in Origin (9.1; 64 bit). FRET imaging and analyses were done as described previously (Kumar et al., 2016). ImageJ was used for basic image processing. All analyses were done using custom-written software (MATLABR2014a; MathWorks; Kumar et al., 2016). All of the graphs were plotted in Origin (9.1; 64 bit). For statistical analysis, data distribution was assumed to be normal, but this was not formally tested. P value for statistical significance was determined from Student's *t* test, and one-way ANOVA analysis was performed to check the statistical significance in Origin software for all the plots in figures.

PREM

Cells were plated on coverslips coated with 10 $\mu\text{g}/\text{ml}$ fibronectin and cultured overnight. Detailed procedures for PREM and immunogold staining were described previously (Svitkina and Borisy, 1998, 2006; Svitkina, 2007, 2009). Briefly, cells were extracted for 2 min at room temperature with 1% Triton X-100 in PEM buffer (100 mM Pipes-KOH, pH 6.9, 1 mM MgCl_2 , and 1 mM EGTA) containing 30% glycerol and 10 μM phalloidin (Sigma-Aldrich). 10 μM phalloidin was added at all subsequent steps before fixation. After three quick rinses with PEM buffer, detergent-extracted cells were incubated with FlnA antibody at 1:200 in PEM buffer for 30 min at room temperature. Samples were rinsed twice in PEM, incubated in the third change of PEM for 15 min, and fixed with 2% glutaraldehyde in PBS for 20 min. Samples were quenched with 2 mg/ml NaBH_4 in PBS, washed three times in PBS, incubated with goat Alexa anti-rabbit secondary antibody (Molecular Probes) for 40 min, washed three times in PBS, blocked in 0.1% bovine serum albumin, incubated overnight with 18-nm gold-conjugated donkey anti-goat antibody (Jackson ImmunoResearch), and washed and fixed with 2% glutaraldehyde. Samples were then fixed with tannic acid and uranyl acetate, critical point dried, coated with platinum and carbon, transferred onto EM grids, and analyzed using a JEM 1011 transmission EM (JEOL USA) operated at 100 kV. Images were captured with an ORIUS 832.10W CCD camera (Gatan) and presented in inverted contrast.

PREM image analysis

Quantification of the SF connection types at the lamella junctions was done on PREM images taken at 20,000 \times magnification. The SFs at the lamella junctions were manually classified into one of three categories: merging, partially merging, or overlapping (not merging). The quantification was done on 36 lamella junctions (14 control cells) and 34 lamella junctions (20 FlnA-depleted cells). Analysis of SF interconnectivity was done on PREM images taken at 20,000 \times magnification using Metamorph imaging software (Molecular Devices). Line scans of 3 μm length (1,200 pixels) were drawn across the cell lamella perpendicular to the direction of SFs. The pixels corresponding to the SFs (actin bundles) appear bright (high pixel intensity), and the gaps between them are dark (low pixel intensity). Continuous bright pixels, which were above average pixel intensity in the line scan, were considered as one actin bundle, or intensity peak. The number of intensity peaks per micrometer of a line scan was counted in line scans of 14 control and 14 FlnA KD

cells and represented as mean \pm SD. Quantification of immunogold particles was done on PREM images taken at $\geq 60,000\times$ magnification after contrast enhancement to distinguish the gold particles from other bright objects. Color labeling of other structures of interest was performed using Hue/Saturation tool in Adobe Photoshop to avoid obscuring the structural details. FlnA immunogold particles located on SFs were classified into two categories: (1) located on crossing actin filaments and (2) located on parallel actin filaments. The gold particles from the two groups were color-labeled in red or green using a brush tool in Adobe Photoshop and counted. In total, we analyzed 4,234 gold particles from a 137- μm^2 SF area of 10 cells.

Online supplemental material

Fig. S1 shows the calibration of custom-made uniaxial stretch device; schematic of control and TS; control talin-CS FRET in unstretched and 10% stretch conditions; estimate of the error in FA angle determination; quantification of FlnA KD from WBs; and various comparisons of morphometric parameters, FRAP curves, and total proteins in control and FlnA KD cells. Fig. S2 shows the difference in localization of various FA-associated proteins within individual adhesions by IF image quantification in scr and FlnA KD cells. Fig. S3 shows additional PREM images of scr and FlnA KD cells and representative line scans, and quantification of talin-TS FRET index and cell orientation (at different time points) of scr and FlnA KD cells in unstretched and 10% stretched conditions.

Acknowledgments

We thank Koen Van Den Dries, Tyler D. Ross, and Tristan P. Driscoll for help in fabricating uniaxial stretcher devices.

This work was supported by the U.S. Department of Defense/Army Research Office through Multidisciplinary University Research Initiative grant W911NF1410403 to M.A. Schwartz and National Institutes of Health grant R01 GM 095977 to T.M. Svitkina.

The authors declare no competing financial interests.

Author contributions: A. Kumar and M.A. Schwartz conceived the project and designed the experiments. A. Kumar carried out the experiments and analyzed the data. M.S. Shutova and T.M. Svitkina carried out EM and data analysis. K. Tanaka made the FlnA-SNAP plasmids. D.V. Iwamoto and D.A. Calderwood provided the shRNA for FlnA KD and EGFP-tagged WT and mutant FlnA constructs. A. Kumar wrote the first draft. M.A. Schwartz revised the manuscript with input from all authors.

Submitted: 15 January 2019

Revised: 3 May 2019

Accepted: 17 June 2019

References

- Atherton, P., B. Stutchbury, D.Y. Wang, D. Jethwa, R. Tsang, E. Meiler-Rodriguez, P. Wang, N. Bate, R. Zent, I.L. Barsukov, et al. 2015. Vinculin controls talin engagement with the actomyosin machinery. *Nat. Commun.* 6:10038. <https://doi.org/10.1038/ncomms10038>
- Austen, K., P. Ringer, A. Mehlich, A. Chrostek-Grashoff, C. Kluger, C. Klingner, B. Sabass, R. Zent, M. Rief, and C. Grashoff. 2015.

- Extracellular rigidity sensing by talin isoform-specific mechanical linkages. *Nat. Cell Biol.* 17:1597–1606. <https://doi.org/10.1038/ncb3268>
- Baldassarre, M., Z. Razinia, C.F. Burande, I. Lamsoul, P.G. Lutz, and D.A. Calderwood. 2009. Filamins regulate cell spreading and initiation of cell migration. *PLoS One*. 4:e7830. <https://doi.org/10.1371/journal.pone.0007830>
- Chan, B.M., and M.E. Hemler. 1993. Multiple functional forms of the integrin VLA-2 can be derived from a single alpha 2 cDNA clone: interconversion of forms induced by an anti-beta 1 antibody. *J. Cell Biol.* 120:537–543. <https://doi.org/10.1083/jcb.120.2.537>
- Chen, Y., A.M. Pasapera, A.P. Koretsky, and C.M. Waterman. 2013. Orientation-specific responses to sustained uniaxial stretching in focal adhesion growth and turnover. *Proc. Natl. Acad. Sci. USA*. 110:E2352–E2361. <https://doi.org/10.1073/pnas.1221637110>
- Choi, C.K., M. Vicente-Manzanares, J. Zareno, L.A. Whitmore, A. Mogilner, and A.R. Horwitz. 2008. Actin and alpha-actinin orchestrate the assembly and maturation of nascent adhesions in a myosin II motor-independent manner. *Nat. Cell Biol.* 10:1039–1050. <https://doi.org/10.1038/ncb1763>
- D'Addario, M., P.D. Arora, J. Fan, B. Ganss, R.P. Ellen, and C.A. McCulloch. 2001. Cytoprotection against mechanical forces delivered through beta 1 integrins requires induction of filamin A. *J. Biol. Chem.* 276:31969–31977. <https://doi.org/10.1074/jbc.M102715200>
- De, R., A. Zemel, and S.A. Safran. 2007. Dynamics of cell orientation. *Nat. Phys.* 3:655–659. <https://doi.org/10.1038/nphys680>
- del Rio, A., R. Perez-Jimenez, R. Liu, P. Roca-Cusachs, J.M. Fernandez, and M.P. Sheetz. 2009. Stretching single talin rod molecules activates vinculin binding. *Science*. 323:638–641. <https://doi.org/10.1126/science.1162912>
- Eghiaian, F., A. Rigato, and S. Scheuring. 2015. Structural, mechanical, and dynamical variability of the actin cortex in living cells. *Biophys. J.* 108:1330–1340. <https://doi.org/10.1016/j.bpj.2015.01.016>
- Faust, U., N. Hampe, W. Rubner, N. Kirchgeßner, S. Safran, B. Hoffmann, and R. Merkel. 2011. Cyclic stress at mHz frequencies aligns fibroblasts in direction of zero strain. *PLoS One*. 6:e28963. <https://doi.org/10.1371/journal.pone.0028963>
- Feng, Y., M.H. Chen, I.P. Moskowitz, A.M. Mendonza, L. Vidali, F. Nakamura, D.J. Kwiatkowski, and C.A. Walsh. 2006. Filamin A (FLNA) is required for cell-cell contact in vascular development and cardiac morphogenesis. *Proc. Natl. Acad. Sci. USA*. 103:19836–19841. <https://doi.org/10.1073/pnas.0609628104>
- Geiger, B., J.P. Spatz, and A.D. Bershadsky. 2009. Environmental sensing through focal adhesions. *Nat. Rev. Mol. Cell Biol.* 10:21–33. <https://doi.org/10.1038/nrm2593>
- Goult, B.T., J. Yan, and M.A. Schwartz. 2018. Talin as a mechanosensitive signaling hub. *J. Cell Biol.* 217:3776–3784. <https://doi.org/10.1083/jcb.201808061>
- Grashoff, C., B.D. Hoffman, M.D. Brenner, R. Zhou, M. Parsons, M.T. Yang, M.A. McLean, S.G. Sligar, C.S. Chen, T. Ha, and M.A. Schwartz. 2010. Measuring mechanical tension across vinculin reveals regulation of focal adhesion dynamics. *Nature*. 466:263–266. <https://doi.org/10.1038/nature09198>
- Heuzé, M.L., I. Lamsoul, M. Baldassarre, Y. Lad, S. Lévêque, Z. Razinia, C. Moog-Lutz, D.A. Calderwood, and P.G. Lutz. 2008. ASB2 targets filamins A and B to proteasomal degradation. *Blood*. 112:5130–5140. <https://doi.org/10.1182/blood-2007-12-128744>
- Himmel, M., A. Ritter, S. Rothenmund, B.V. Pauling, K. Rottner, A.R. Gingras, and W.H. Ziegler. 2009. Control of high affinity interactions in the talin C terminus: how talin domains coordinate protein dynamics in cell adhesions. *J. Biol. Chem.* 284:13832–13842. <https://doi.org/10.1074/jbc.M900266200>
- Hirata, H., H. Tatsumi, C.T. Lim, and M. Sokabe. 2014. Force-dependent vinculin binding to talin in live cells: a crucial step in anchoring the actin cytoskeleton to focal adhesions. *Am. J. Physiol. Cell Physiol.* 306:C607–C620. <https://doi.org/10.1152/ajpcell.00122.2013>
- Hsu, H.J., C.F. Lee, A. Locke, S.Q. Vanderzyl, and R. Kaunas. 2010. Stretch-induced stress fiber remodeling and the activations of JNK and ERK depend on mechanical strain rate, but not FAK. *PLoS One*. 5:e12470. <https://doi.org/10.1371/journal.pone.0012470>
- Humphrey, J.D., E.R. Dufresne, and M.A. Schwartz. 2014. Mechano-transduction and extracellular matrix homeostasis. *Nat. Rev. Mol. Cell Biol.* 15:802–812. <https://doi.org/10.1038/nrm3896>
- Iwamoto, D.V., A. Huehn, B. Simon, C. Huet-Calderwood, M. Baldassarre, C.V. Sindelar, and D.A. Calderwood. 2018. Structural basis of the filamin A actin-binding domain interaction with F-actin. *Nat. Struct. Mol. Biol.* 25:918–927. <https://doi.org/10.1038/s41594-018-0128-3>
- Kainulainen, T., A. Pender, M. D'Addario, Y. Feng, P. Lekic, and C.A. McCulloch. 2002. Cell death and mechanoprotection by filamin A in connective tissues after challenge by applied tensile forces. *J. Biol. Chem.* 277:21998–22009. <https://doi.org/10.1074/jbc.M200715200>
- Kaneko, D., Y. Sasazaki, T. Kikuchi, T. Ono, K. Nemoto, H. Matsumoto, and Y. Toyama. 2009. Temporal effects of cyclic stretching on distribution and gene expression of integrin and cytoskeleton by ligament fibroblasts in vitro. *Connect. Tissue Res.* 50:263–269. <https://doi.org/10.1080/03008200902846270>
- Kiema, T., Y. Lad, P. Jiang, C.L. Oxley, M. Baldassarre, K.L. Wegener, I.D. Campbell, J. Ylänne, and D.A. Calderwood. 2006. The molecular basis of filamin binding to integrins and competition with talin. *Mol. Cell.* 21:337–347. <https://doi.org/10.1016/j.molcel.2006.01.011>
- Klapholz, B., and N.H. Brown. 2017. Talin - the master of integrin adhesions. *J. Cell Sci.* 130:2435–2446. <https://doi.org/10.1242/jcs.190991>
- Kumar, A., M. Ouyang, K. Van den Dries, E.J. McGhee, K. Tanaka, M.D. Anderson, A. Groisman, B.T. Goult, K.I. Anderson, and M.A. Schwartz. 2016. Correction: Talin tension sensor reveals novel features of focal adhesion force transmission and mechanosensitivity. *J. Cell Biol.* 214:231. <https://doi.org/10.1083/jcb.20151001207062016c>
- Kumar, A., K.L. Anderson, M.F. Swift, D. Hanein, N. Volkmann, and M.A. Schwartz. 2018. Local Tension on Talin in Focal Adhesions Correlates with F-Actin Alignment at the Nanometer Scale. *Biophys. J.* 115:1569–1579. <https://doi.org/10.1016/j.bpj.2018.08.045>
- Lad, Y., T. Kiema, P. Jiang, O.T. Pentikäinen, C.H. Coles, I.D. Campbell, D.A. Calderwood, and J. Ylänne. 2007. Structure of three tandem filamin domains reveals auto-inhibition of ligand binding. *EMBO J.* 26:3993–4004. <https://doi.org/10.1038/sj.emboj.7601827>
- Lee, C.F., C. Haase, S. Deguchi, and R. Kaunas. 2010. Cyclic stretch-induced stress fiber dynamics - dependence on strain rate, Rho-kinase and MLCK. *Biochem. Biophys. Res. Commun.* 401:344–349. <https://doi.org/10.1016/j.bbrc.2010.09.046>
- Nagayama, K., Y. Kimura, N. Makino, and T. Matsumoto. 2012. Strain waveform dependence of stress fiber reorientation in cyclically stretched osteoblastic cells: effects of viscoelastic compression of stress fibers. *Am. J. Physiol. Cell Physiol.* 302:C1469–C1478. <https://doi.org/10.1152/ajpcell.00155.2011>
- Nakamura, F., M. Song, J.H. Hartwig, and T.P. Stossel. 2014. Documentation and localization of force-mediated filamin A domain perturbations in moving cells. *Nat. Commun.* 5:4656. <https://doi.org/10.1038/ncomms5656>
- Patel, B., A.R. Gingras, A.A. Bobkov, L.M. Fujimoto, M. Zhang, R.C. Lidington, D. Mazzeo, J. Emsley, G.C. Roberts, I.L. Barsukov, and D.R. Critchley. 2006. The activity of the vinculin binding sites in talin is influenced by the stability of the helical bundles that make up the talin rod. *J. Biol. Chem.* 281:7458–7467. <https://doi.org/10.1074/jbc.M508058200>
- Pinto, V.I., V.W. Senini, Y. Wang, M.P. Kazembe, and C.A. McCulloch. 2014. Filamin A protects cells against force-induced apoptosis by stabilizing talin- and vinculin-containing cell adhesions. *FASEB J.* 28:453–463. <https://doi.org/10.1096/fj.13-233759>
- Priddle, H., L. Hemmings, S. Monkley, A. Woods, B. Patel, D. Sutton, G.A. Dunn, D. Zicha, and D.R. Critchley. 1998. Disruption of the talin gene compromises focal adhesion assembly in undifferentiated but not differentiated embryonic stem cells. *J. Cell Biol.* 142:1121–1133. <https://doi.org/10.1083/jcb.142.4.1121>
- Razinia, Z., T. Mäkelä, J. Ylänne, and D.A. Calderwood. 2012. Filamins in mechanosensing and signaling. *Annu. Rev. Biophys.* 41:227–246. <https://doi.org/10.1146/annurev-biophys-050511-102252>
- Shao, Y., X. Tan, R. Novitski, M. Muqaddam, P. List, L. Williamson, J. Fu, and A.P. Liu. 2013. Uniaxial cell stretching device for live-cell imaging of mechanosensitive cellular functions. *Rev. Sci. Instrum.* 84:114304. <https://doi.org/10.1063/1.4832977>
- Smith, M.A., E. Blankman, M.L. Gardel, L. Luettjohann, C.M. Waterman, and M.C. Beckerle. 2010. A zyxin-mediated mechanism for actin stress fiber maintenance and repair. *Dev. Cell.* 19:365–376. <https://doi.org/10.1016/j.devcel.2010.08.008>
- Svitkina, T. 2007. Electron microscopic analysis of the leading edge in migrating cells. *Methods Cell Biol.* 79:295–319. [https://doi.org/10.1016/S0091-679X\(06\)79012-4](https://doi.org/10.1016/S0091-679X(06)79012-4)
- Svitkina, T. 2009. Imaging cytoskeleton components by electron microscopy. *Methods Mol. Biol.* 586:187–206. https://doi.org/10.1007/978-1-60761-376-3_10

- Svitkina, T.M. 2018. Ultrastructure of the actin cytoskeleton. *Curr. Opin. Cell Biol.* 54:1–8. <https://doi.org/10.1016/j.ceb.2018.02.007>
- Svitkina, T.M., and G.G. Borisy. 1998. Correlative light and electron microscopy of the cytoskeleton of cultured cells. *Methods Enzymol.* 298: 570–592. [https://doi.org/10.1016/S0076-6879\(98\)98045-4](https://doi.org/10.1016/S0076-6879(98)98045-4)
- Svitkina, T.M., and G.G. Borisy. 2006. Correlative Light and Electron Microscopy of the Cytoskeleton. In *Cell Biology*. Third edition. J.E. Celis, editor. Academic Press, Burlington. 277–285. <https://doi.org/10.1016/B978-012164730-8/50156-8>
- Vogel, V., and M. Sheetz. 2006. Local force and geometry sensing regulate cell functions. *Nat. Rev. Mol. Cell Biol.* 7:265–275. <https://doi.org/10.1038/nrml1890>
- Wang, J.H., G. Yang, Z. Li, and W. Shen. 2004. Fibroblast responses to cyclic mechanical stretching depend on cell orientation to the stretching direction. *J. Biomech.* 37:573–576. <https://doi.org/10.1016/j.jbiomech.2003.09.011>
- Zhou, A.X., J.H. Hartwig, and L.M. Akyürek. 2010. Filamins in cell signaling, transcription and organ development. *Trends Cell Biol.* 20:113–123. <https://doi.org/10.1016/j.tcb.2009.12.001>